Chapter

A Simple and "Green" Technique to Synthesize Metal Nanocolloids by Ultrashort Light Pulses

Jesica María José Santillán, David Muñetón Arboleda, Valeria Beatriz Arce, Lucía Beatriz Scaffardi and Daniel Carlos Schinca

Abstract

In this chapter Ag, Ni and Fe nanocolloids synthesized by "green" ultrashort pulse laser ablation of solid metal targets using different pulse energies and liquid media are characterized by different techniques. Optical extinction spectroscopy (OES), micro-Raman spectroscopy (MRS), transmission electron microscopy (TEM) and electron diffraction (ED) were independently used to analyze optical, morphological and compositional properties of the generated nanocolloids. In a deeper way, the stability characteristics of Ag nanocolloids in aqueous solutions with different stabilizers were studied owing to their potential use in biocompatible compounds. Besides, due to their interesting applications, few atoms Ag nanoclusters (NCs) were synthesized using the same ablation technique, analyzing their fluorescent and photocatalytic properties. On the other hand, to expand the characterization of the nanocolloids, their magnetic behavior was inspected for the Ni and Fe by vibrating sample magnetometry (VSM).

Keywords: nanocolloids, green synthesis, metal nanoparticles, nanoclusters, femtosecond laser ablation

1. Introduction

Interest in metal nanomaterials synthesis has grown rapidly in the last years due to their particular physical and chemical properties arising from atom interaction and quantum confinement at the nanoscale. Their applicability spans different fields of science and technology [1–3]. It is known that chemical synthesis methods tend to yield highly monodisperse colloidal suspensions, but mixed with unwanted chemical precursors, which often leads to purification steps to remove the chemical by-products and may derive in expensive and complicated procedures. For this reason, femtosecond laser ablation synthesis in solution (FLASiS) has emerged as a competitive and alternative method for synthesizing metallic nanomaterials without the intervention of unwanted chemical compounds. Besides, it has the ability of producing small spherical nanoparticles (NPs) [4, 5] as well as few atoms metal NCs [6].

In this chapter, different independent techniques are used to characterize the ablated nanomaterials. Altogether, they retrieve complementary and interrelated information about different NPs characteristics. TEM provides knowledge about morphology, internal structure, sphericity and size distribution in a small piece of sample. ED is an established technique that can identify different phase compositions and crystallinity type. Optical spectroscopy techniques (absorption, extinction, scattering and fluorescence) have the ability to interact with a very large number of NPs (on the order of $10^{12}\,cm^{-3}$), enhancing statistics. OES together with Mie theory yields information related to size distribution, sphericity, configuration and composition of the NPs in the colloidal sample. MRS retrieves information about possible interactions between stabilizer solution molecules adsorbed to the NPs walls and the NP itself. In particular, for Ag nanocolloids generated in aqueous solutions with small concentrations of stabilizers, long term stability characteristics were studied, aiming to possible applications in biocompatible antibacterial compounds. For the case of magnetic metals NPs, magnetic nanocolloid properties were studied using VSM. Finally, fluorescent and photocatalytic properties of few atoms Ag NCs were analyzed.

2. FLASiS as a green route for NPs and few atoms NCs synthesis

Traditional techniques for metal NPs synthesis have relied on chemical reaction associated to metallic salt dissociation [7], which suitably reduce to form metallic atoms.

FLASiS is based on the incidence of a focused laser pulse on a bulk target immersed in a liquid [8, 9] (**Figure 1**). The produced plasma plume that contains the ablated material expands into the surrounding liquid and generates a cavitation bubble, which acts as a reactor for NPs formation through condensation of atoms [8]. This process produces ions and atoms that reach different nucleation stages, and generates large NPs (radii >20 nm), medium NPs (2 nm < radii <20 nm), small NPs (1 nm < radii <2 nm) together with very small NCs (radii <1 nm) [6–10].

Since FLASiS is capable of synthesizing NPs directly in a selected liquid without producing unwanted compounds in the solution, it is considered a "green" technique. As the schematic in **Figure 1** depicts, the NPs generated during FLASiS

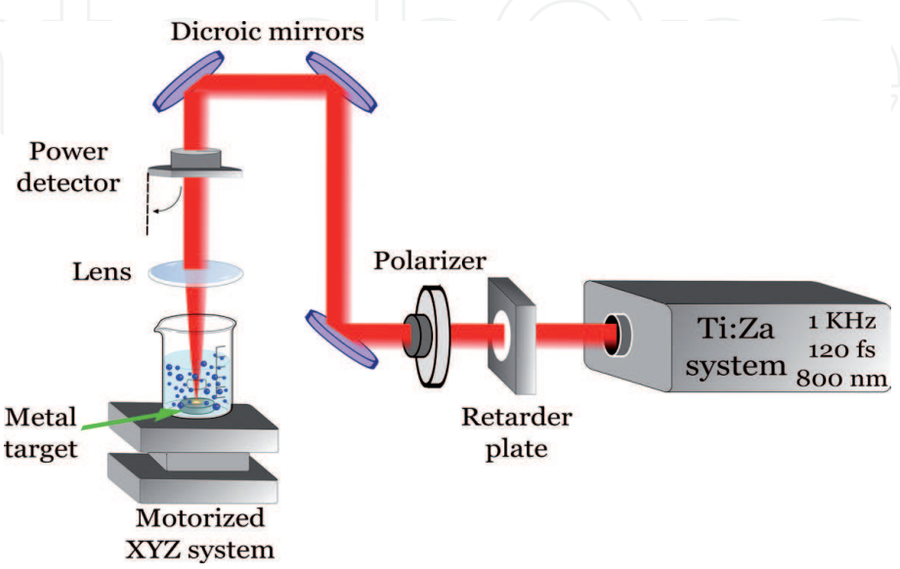

Figure 1.
General schematic of the experimental setup for FLASiS. The cell containing the target is placed over a XYZ micro translational platform.

remain in the liquid, forming a suspension with a NPs concentration dependent on laser pulse energy and ablation time.

2.1 Characterization of Ag nanocolloids synthesized by FLASiS and chemical route in aqueous solutions of trisodium citrate (TSC) and starch (st)

Ag NPs have attractive scientific interest due of their broad perspectives in biosensors [11], food production [12], water purification [13], antimicrobial and antiviral agents [14, 15], among others. In these areas of research and development, the ability to control size, shape, functionalization and stability of Ag NPs is essential for expanding their possible applicability. For this goal, typical methods are based on chemical reduction of salts in solution, commonly used for providing good size control and resulting in final spherical shape. However, this approach leaves chemical residuals in the final colloidal suspension, which may be toxic for certain applications, thus adding an extra difficulty in sample purification. In this sense, FLASiS has become an alternative method for overcoming the mentioned drawback.

Figure 2 shows experimental and theoretical extinction spectra of Ag nanocolloids prepared by salt reduction (short dashed line) as well as those generated by FLASiS with 100 μJ (dashed line) and 500 μJ (dashed dotted line) pulse energies, with two different stabilizers 1 mM TSC (a) and 1% soluble st (b) solutions. These spectra are normalized to plasmon maximum. The theoretical fits (dotted lines) are determined using OES, which is based in the calculation of the Mie theory for metal spherical NPs [17, 18] with log-normal size distributions (insets).

Nanocolloids stabilized with TSC show a small redshift in peak position respect to the typical plasmonic resonance band at 395 nm, indicating the existence of $Ag@Ag_2O$ NPs [19, 20] with a log-normal shell thickness distribution in the three samples obtained. Nanocolloids obtained by FLASiS have a larger contribution of $Ag@Ag_2O$ NPs than the sample generated by chemical synthesis (**Figure 2(a)**). This finding agrees with the known fact that, during laser ablation of a metal target in liquid media, an oxidation-reduction process occurs, producing an oxide coating growth around the NPs [20, 21].

On the other hand, the st stabilized nanocolloids obtained by salt reduction have a large redshift at the peak position compared to FLASiS (**Figure 2(b)**), due to a larger oxide shell thickness around the NPs.

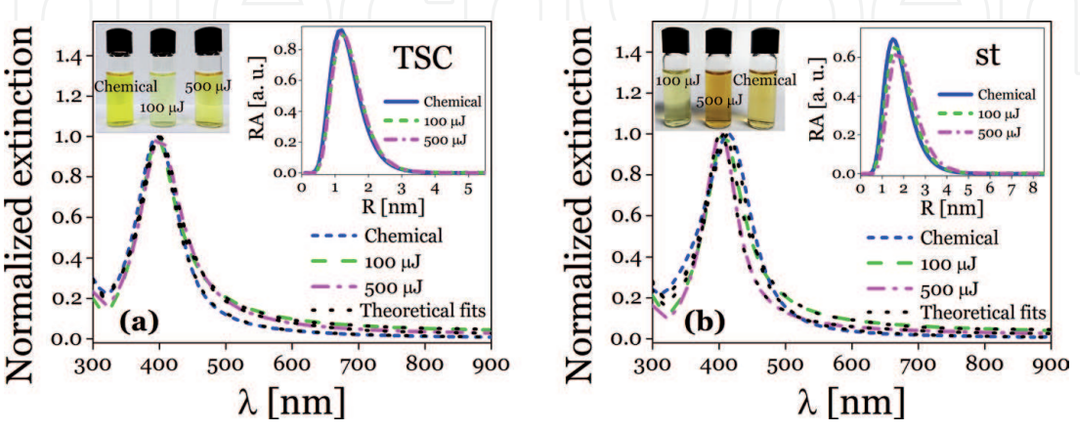

Figure 2.
Normalized experimental optical extinction spectra together with theoretical fits (dotted lines) of freshly prepared Ag nanocolloids obtained by silver salt reduction and FLASiS with 100 μJ and 500 μJ pulse energies, using 1 mM TSC (a) and 1% soluble st (b) solutions. Insets exhibit the relative abundances (RA) of the NPs present in the nanocolloids used to fitting the experimental spectra (reprinted with permission from [16] copyright 2018 Elsevier).

For the fitting of the spectra using Mie theory, three types of species were considered: Ag, Ag@Ag_2O, and in a smaller amount hollow Ag NPs. It is important to recall that these types of nanostructures are prone to occur for pulse laser ablation conditions [9, 22].

The morphological characterization and sizing of NPs synthesized by both methods was performed using TEM.

Figure 3 presents TEM images of Ag nanocolloids obtained by FLASiS with 500 μJ pulse energy in 1 mM TSC (a) and 1% soluble st (c) solutions, and prepared by salt reduction in 1 mM TSC (b) and 1% soluble st (d) solutions. All images are typical panoramic views with predominant spherical shape NPs. Right insets in panels (a) and (b) are lattice-resolved images of a single NP with Bragg planes identified as (200) of Ag FCC crystal, whereas the right inset in panel (c) exhibits the presence of hollow NPs. Left insets in the panels (a) - (d) are size histograms taken from several images. The results given by TEM are in good agreement with those obtained by OES from the fitting of the spectra.

Micro-Raman spectroscopy was conducted on the FLASiS samples to assess the existence of silver oxide species. **Figure 4** shows Raman spectra of a dried drop of Ag nanocolloids prepared by FLASiS with 500 μJ pulse energy in 1 mM TSC (a) and

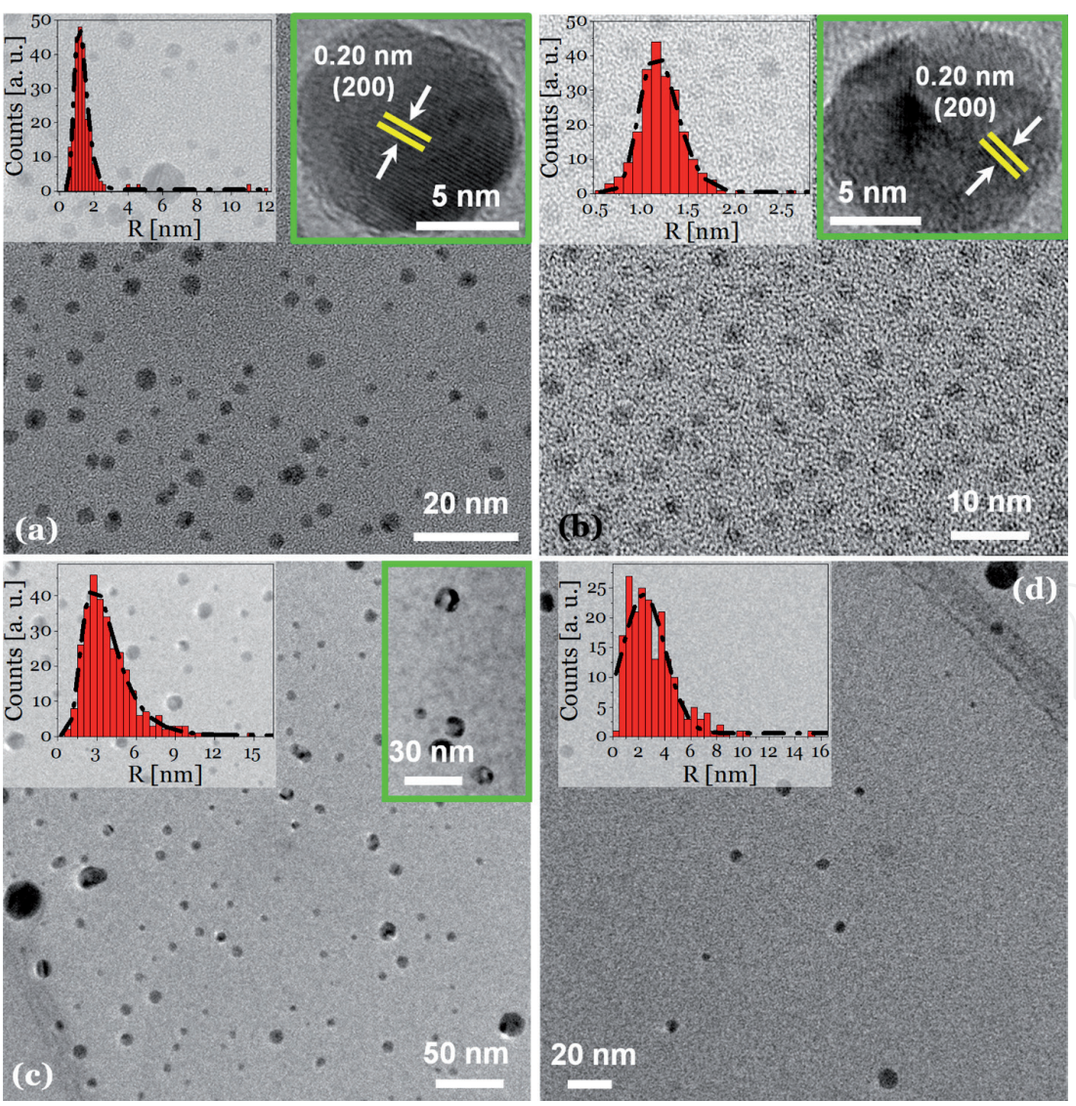

Figure 3.
TEM images of the NPs present in the Ag nanocolloids generated by FLASiS (500 μJ pulse energy) in a 1 mM TSC solution (a), 1% soluble st solution (c), prepared by chemical route in 1 mM TSC (b) and 1% soluble st (d) solutions (reprinted with permission from: [16] Copyright 2018 Elsevier and [23] copyright 2017 ACS).

1% soluble st (b) solutions, acquired in different regions of the sample. Several peaks corresponding to Ag_2O (asterisk) may be recognized in both samples. Raman signals at 240 cm^{-1} and 490 cm^{-1} are typical Ag-O stretching/bending modes in Ag_2O [24]. Besides, characteristic peaks of the metallic NP interaction with each stabilizer (TSC (diamond) and st (full circle)) are also observed [25–27].

Stability analysis was conducted on Ag nanocolloids produced by FLASiS (100 μJ and 500 μJ pulse energies) and chemical route with 1 mM TSC (**Figure 5(a)**) and 1% soluble st (**Figure 5(b)**) solutions. Plasmon resonance position and full width at half maximum (FWHM) for experimental spectra, were measured for freshly prepared samples and followed during several weeks (even up to one-year old samples with TSC stabilizer). The shift of plasmon peak (upper panel) and the behavior of FWHM (lower panel) of the experimental spectra in **Figure 5**, are represented by geometric symbols, while the lines are drawn to visually follow the evolution of both parameters.

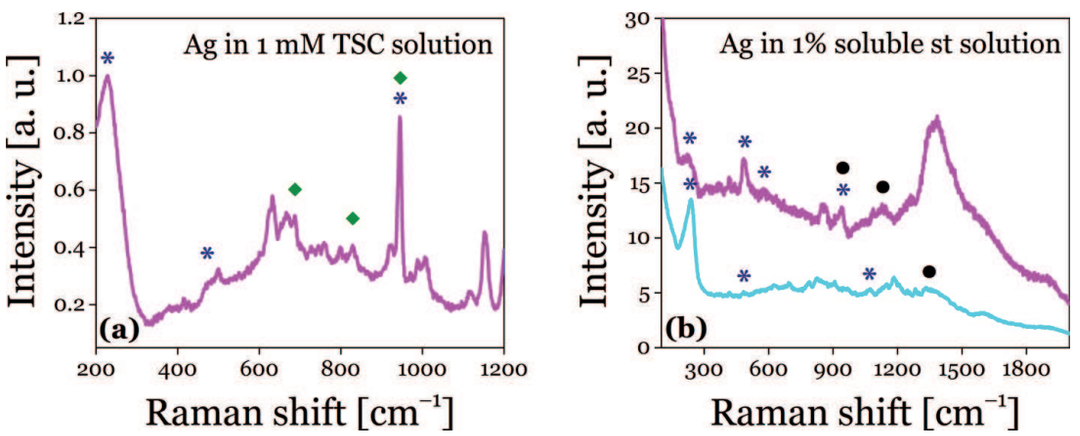

Figure 4.
Raman spectra of Ag nanocolloids obtained by FLASiS with 500 μJ pulse energy in 1 mM TSC (a) and 1% soluble st (b) solutions acquired at different sites in the samples (reprinted with permission from: [16] Copyright 2018 Elsevier and [23] copyright 2017 ACS).

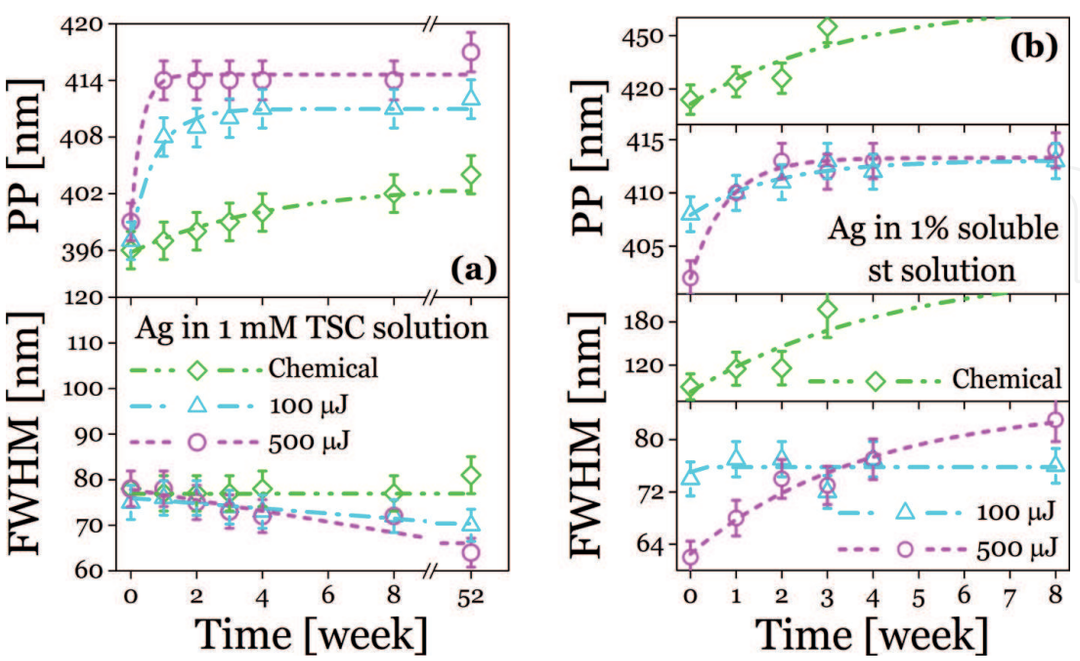

Figure 5.
Peak position (PP) and FWHM of the experimental extinction spectra of Ag nanocolloids synthesized by FLASiS (100 μJ and 500 μJ pulse energies) and salt reduction in 1 mM TSC (a) and 1% soluble st (b) solutions. These plasmonic characteristics were monitored during several weeks (reprinted with permission from: [16] Copyright 2018 Elsevier and [23] Copyright 2017 ACS).

From the plots in the upper panel (a), it can be seen that samples obtained by FLASiS in 1 mM TSC solution, reach their saturation regime at the second week (fast rate). However, nanocolloid produced by salt reduction method seems to reach saturation at times beyond one year (slow rate).

Nanocolloids synthesized by FLASiS still after one year show a clear plasmonic band without signs of agglomeration, indicating the excellent properties of TSC as stabilizer. Long-term stability results are similar to those for salt reduction chemical synthesis using TSC as stabilizer.

On the other hand, FWHM (lower panel (a)) reveals a very stable regime for the salt reduction synthesis during one year, whereas for FLASiS samples it presents a decrease, indicating a slight narrowing of the plasmon resonance.

For the case of st used as stabilizer (b), the monitoring of plasmon resonance peak position and FWHM show that FLASiS samples stabilize much faster than those produced by salt reduction. It is also observed that low energy pulses seem to produce more stable nanocolloids than higher energy pulses. This larger stability could be due to some kind of laser-induced NPs surface modification with amylose that avoids coalescence and sets a limit to their size. In contrast to all these cases, no stable suspensions are obtained for salt reduction, because plasmon peak is continuously red-shifted and FWHM increases without showing stationary behavior.

2.2 Synthesis and characterization of metal nanocolloids with magnetic properties (Ni and Fe)

In recent years, one of the most active topics in nanotechnology is the synthesis, characterization and functionalization of magnetic NPs. The interest in this type of NPs is due to their wide applications in areas of diagnosis and therapy in biomedicine [28, 29], as contrast agents in magnetic resonance imaging [30], for drug administration [31], as catalysts [32, 33], among others.

In this Subsection the characterization of Ni and Fe nanocolloids synthesized by FLASiS with different pulse energies and in different liquid media is addressed. Independent characterization techniques such as OES, TEM, ED, MRS, and VSM are used, which provide complementary and interrelated information.

2.2.1 Ni nanocolloids synthesized by FLASiS in n-heptane and water

In the synthesis of nanomaterials, Ni nanocolloids have attracted scientific interest because of their extensive prospects in catalysts [32, 33], information storage [32], magnetic behavior [34], biomedicine [35], among others.

Although there are different studies of the production of Ni colloidal suspensions by laser ablation, few of these have been in the femtosecond regime. Experimental and theoretical extinction spectra of Ni nanocolloids synthesized by FLASiS with 100 μJ pulse energy in *n*-heptane and water are observed in **Figure 6**. These spectra are recorded immediately after synthesis and normalized at $\lambda = 340\ \text{nm}$. For the case of nanocolloid in *n*-heptane, the log-normal distribution (inset in **Figure 6(a)**) is formed by Ni NPs with modal radius of 2.5 nm and 10 nm, together with hollow Ni NPs with external modal radius of 6.6 nm (10% shell), 12 nm (20% shell) and 15.6 nm (4% shell). However, for the case of the nanocolloid obtained in water, the multimodal size distribution (inset in **Figure 6(b)**) shows the presence of Ni@NiO NPs (short dashed line), NiO@Ni (dashed dotted line) and hollow Ni (short dashed dotted line), with sizes similar to that determined for *n*-heptane but shifted to higher values of external radii due to the presence of oxide shells around the NPs. Each one of the mentioned species influences the extinction spectrum in specific and distinct regions, in such a way that the combination of

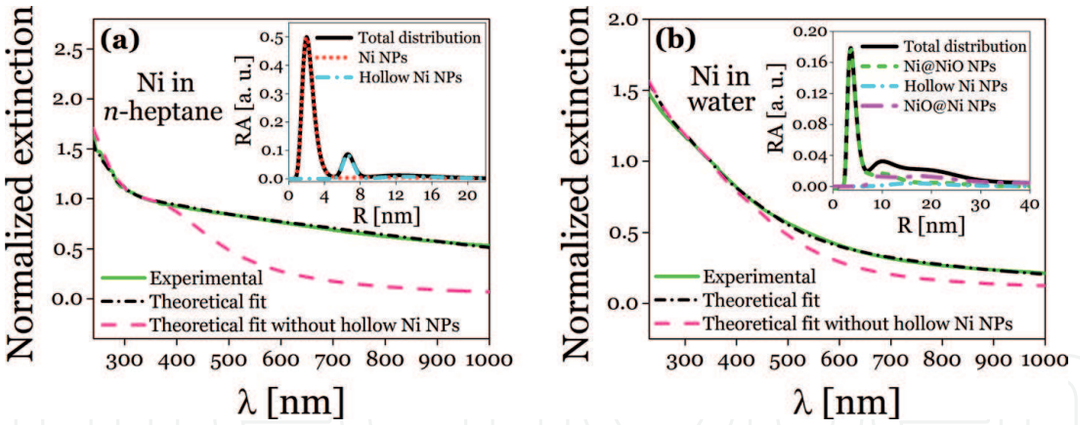

Figure 6.
Experimental (solid line) and theoretical (dashed dotted line) extinction spectra of the Ni nanocolloids in (a) n-heptane and (b) water. The dashed line represents the theoretical fit without considering the presence of hollow Ni NPs. The insets show the RA of the different species of NPs present in the nanocolloids (reprinted with permission from [18] Copyright 2015 ASC).

structures, sizes, and relative abundances derived from the optimum fit constitute a unique set of fitting parameters, showing the high sensitive of OES technique [18].

Morphology analysis of NPs in the Ni nanocolloids was performed using TEM. **Figure 7** presents TEM images of the nanocolloids synthesized in *n*-heptane ((a) and (b)) and water ((c) and (d)). Panel (a) is a panoramic view of Ni and hollow Ni NPs together with an enlargement of a NP with the latter structure indicated by the dotted line. Panel (b) images a Ni NP from a different region. Panel (c) is a panoramic view where NPs with different structures are observed, and panel (d) contains enlargements where the Bragg planes of NiO can be seen. ED is performed to phase identification of the NPs. Panel (e) shows a representative ED pattern indexed with the reflection lines of NiO (cubic, $Fm\ \overline{3}\ m$, JCPDS #75-0197) and Ni (cubic, $Fm\overline{3}m$, JCPDS # 04-0850) for the Ni nanocolloid in water. ED rings are marked according to the panel table (f), where the Miller indices (h, k, l) and interplane distances (d) are indicated.

Insets in panels (b) and (c) present histograms of radii corresponding to a statistic performed on several TEM images, where the results are fitted by two log-normal size distributions that describe the most prominent characteristics of the size distribution histogram. The results obtained through TEM analysis for both nanocolloids corroborate the morphological determinations achieved through OES.

Magnetic response of Ni nanocolloids synthesized by FLASiS in *n*-heptane and water was determined by the VSM technique. **Figure 8** exhibits this magnetic response as a function of the applied field. It is observed that the nanocolloid in *n*-heptane exhibits a greater magnetic response than in water. The above is concluded comparing the saturation magnetization and coercivity of 7.5 emu g^{-1} and 90 Oe in *n*-heptane, and 4.4 emu g^{-1} and 61 Oe in water, respectively.

The fitting curve in **Figure 8** agrees with the superparamagnetic behavior of the nanocolloids, corresponding to a Langevin function weighted with a log-normal distribution of magnetic moments ($g(\mu)$) and a linear contribution proportional to the susceptibility (χ_p) of the field. This function is given by Eq. 1:

$$M = N_d \int_0^\infty \mu \left[\coth\left(\frac{\mu\mu_o H}{k_B T} \right) - \frac{k_B T}{\mu\mu_0 H} \right] g(\mu) d\mu + \chi_p H \qquad (1)$$

where, the mean magnetic moment ($\mu = \mu_o e^{\sigma^2/2}$) is obtained from the fitted parameters of the log-normal (median μ_o and dispersion σ) and the saturation magnetization is given by $M_S = N_d \mu$, where N_d is the number density of NPs.

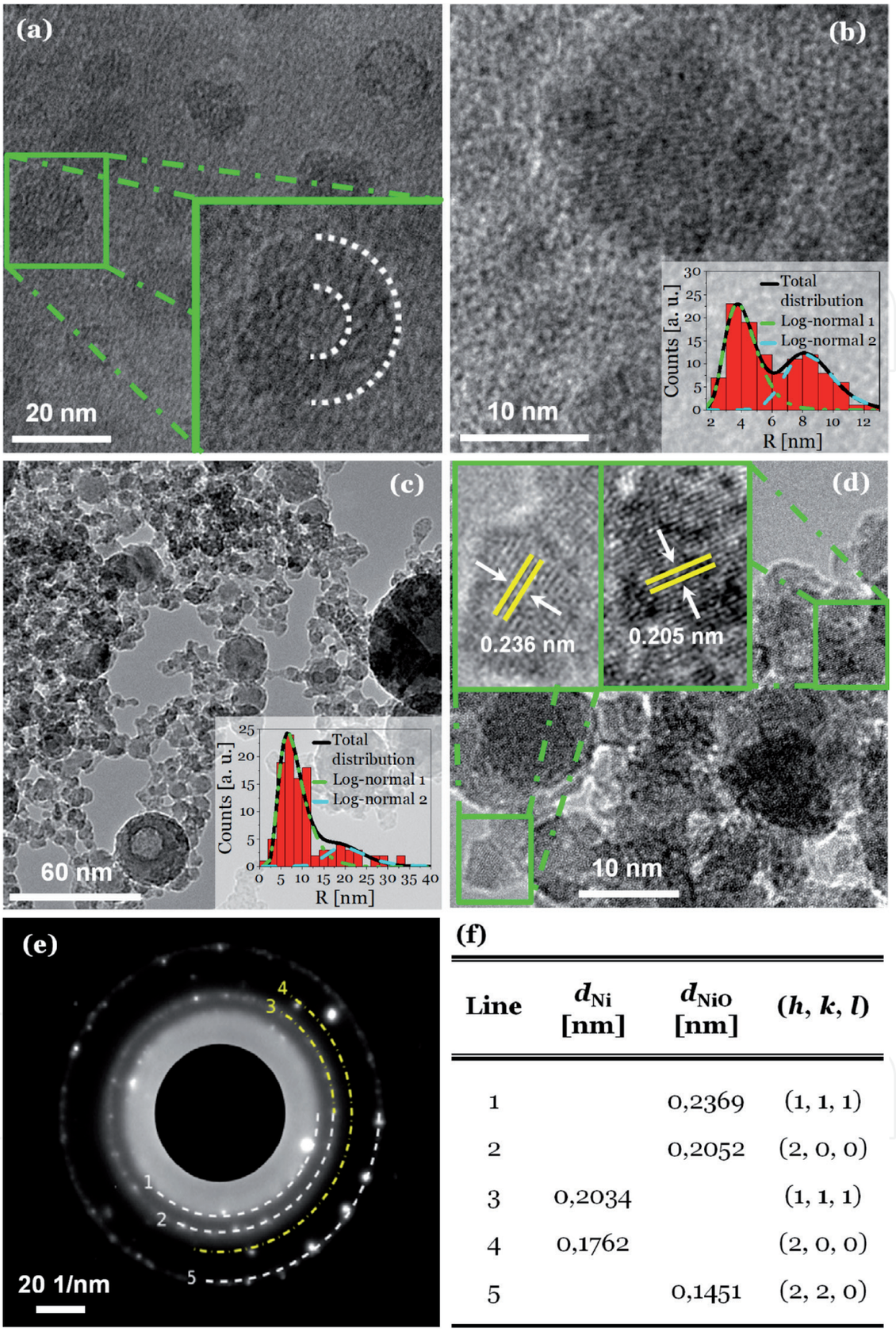

(f)

Line	d_{Ni} [nm]	d_{NiO} [nm]	(*h*, *k*, *l*)
1		0,2369	(1, 1, 1)
2		0,2052	(2, 0, 0)
3	0,2034		(1, 1, 1)
4	0,1762		(2, 0, 0)
5		0,1451	(2, 2, 0)

Figure 7.
TEM images of the NPs present in the Ni nanocolloids synthesized in n*-heptane (a) and (b), and water (c) and (d). (e) ED pattern indexed with the reflection lines belonging to NiO (lines 1, 2 and 5) and Ni (lines 3 and 4) according to table (f) for the Ni nanocolloid in water (reprinted with permission from [18] Copyright 2015 ASC).*

From the fit of the experimental data, the log-normal size distributions are determined (inset) considering that each NP of volume V is magnetized as $M_S = \mu / V$. Furthermore, r_M and r_T are calculated taking into account the

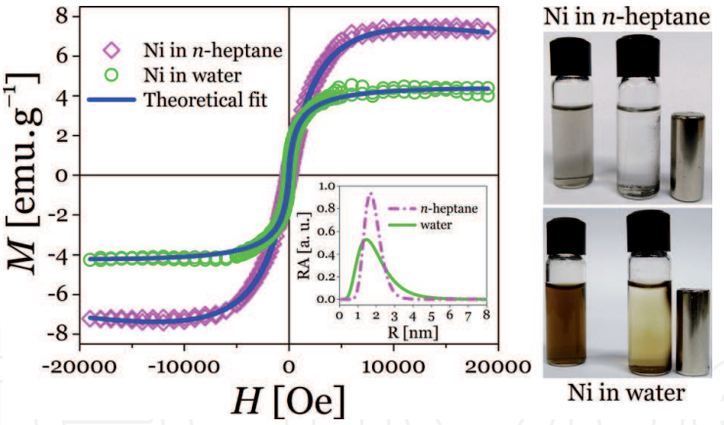

Figure 8.
Experimental magnetization curves and Langevin fitting of Ni nanocolloids in n-heptane and in water. The inset shows the size distribution for each nanocolloid. At the right: photographs of the colloidal suspensions showing the magnetic effect on the NPs exerted by a NdFeB magnet.

experimental and theoretical magnetization, respectively. The difference between these two values corresponds to the size of the magnetically NiO oxide shell frustrated layer, which does not present any type of magnetization. The size distributions are determined without considering hollow NPs or structures that present higher oxidation. Therefore, this determination is an estimative measurement that complements the characterization by OES and TEM.

2.2.2 Fe nanocolloids synthesized by FLASiS in water and ethanol

Synthesis of metallic Fe NPs and their dispersion in various liquid media is of great interest in the field of nano-magnetic materials, owing to great potential in biomedical applications [28–31]. The main routes for the synthesis of Fe NPs have been through wet chemistry [36–38]. Depending on the technique, NPs with different morphological and physicochemical characteristics can be obtained. In the case of FLASiS, the different processes that eventually occur lead to the formation of self-organized spherical nanostructures with different morphological, structural, compositional, and size characteristics compared with those generated with chemical techniques. **Figure 9** presents the experimental extinction spectra of the different Fe nanocolloids obtained by FLASiS using pulse energies of 70 μJ, 300 μJ and 700 μJ in water and ethanol. All spectra show an overall decrease in optical extinction as laser energy decreases, indicating, as expected, a lesser amount of ablated material. This is also qualitatively supported by the decreasing coloration of the colloidal suspensions (insets in **Figure 9**).

The extinction spectra of the Fe nanocolloids lack the characteristic plasmonic resonance exhibited by some metals, as seen above for the case of Ag (subsection 2.1.) and Ni (subsection 2.2.1.). This fact makes it difficult to fully characterize these suspensions by OES.

However, it can be observed that the spectra decrease monotonically in both media, except for the region from 300 nm up to 400 nm, in which the spectral behavior remains shoulder-shaped. This may be due to the presence of NPs with sizes greater than 20 nm. Although the number density of these NPs may be low, they have large enough cross-section, so their contribution is observable in the extinction spectra.

Furthermore, for ethanol, the formation of NPs with Fe_3C is highly probable, due to the binding of free carbons to Fe NPs during the ablation process at the plasma-liquid interface [8]. This is concluded from the fact that Fe_3C has an absorption band in the range of 300 nm - 400 nm, as can be seen in panel (b). This

is due to the reactivity that such solvent has with Fe atoms at the high temperatures present in the plasma during FLASiS. Similar results are reported by other authors [40] who assign this band to the presence of Fe_3C in colloids.

From the spectroscopic results it can be concluded that the colloids have very similar composition. Therefore, from this point only the samples obtained with 700 μJ pulse energy are analyzed.

Figure 10 exhibits Raman spectra of the Fe nanocolloids in water (a) and ethanol (b), recorded in different regions of the sample. In both cases, it can be seen that depending on the local measurement area, the spectra show Raman signals of magnetite (Fe_3O_4 , full circle), hematite ($\alpha - Fe_2O_3$, asterisk) or mixtures of them. For the case of water, maghemite ($\lambda - Fe_2O_3$, diamond) signals are also detected.

Figure 11 shows TEM images of the Fe nanocolloids in water (a) and ethanol (b). Panel (a) is a panoramic view that includes core@shell NPs indicated with dashed line circles. An enlargement of a hollow Fe NP is observed in the inset. Panel (b) presents a group of NPs of typical size in ethanol. ED measurements are

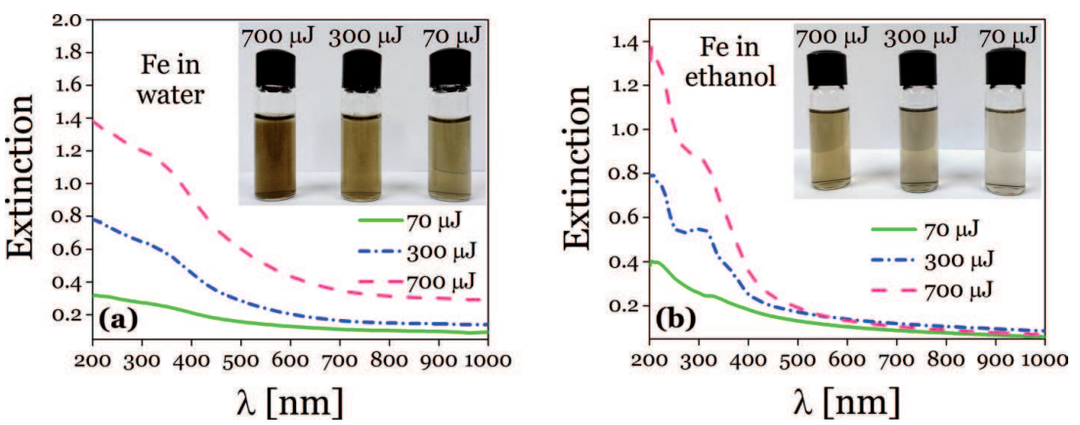

Figure 9.
Experimental extinction spectra of Fe nanocolloids synthesized by FLASiS in (a) water and (b) ethanol, with three different pulse energies. The insets exhibit photographs of the nanocolloids in each solvent (reprinted with permission from [39] copyright 2017 Wiley-VCH).

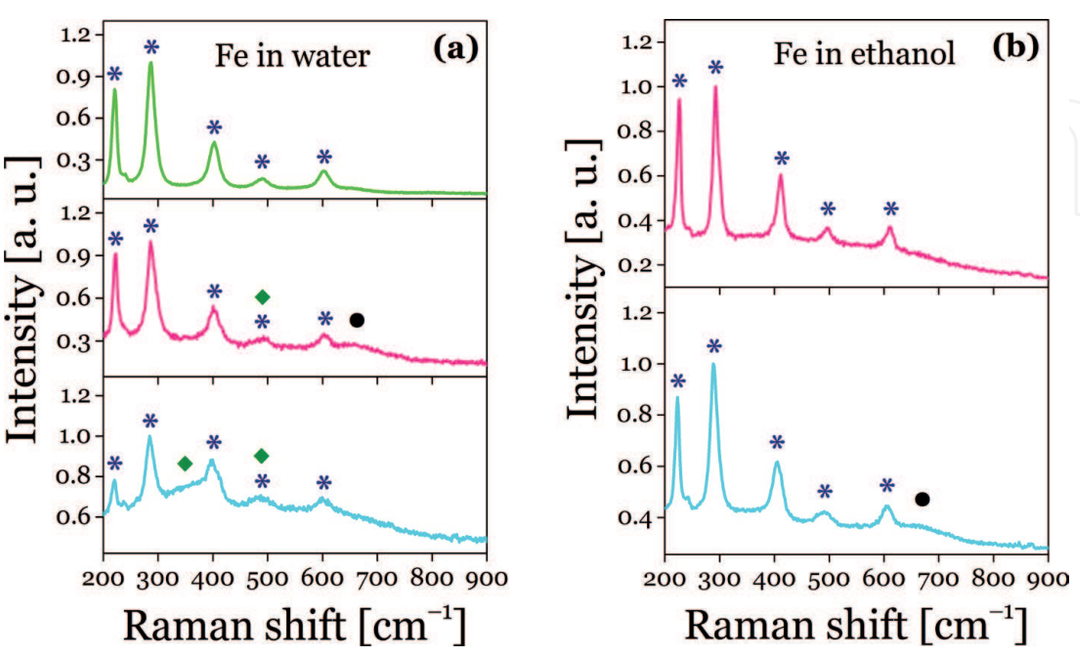

Figure 10.
Raman spectra of Fe nanocolloids in water (a) and ethanol (b) recorded at different points in the samples (reprinted with permission from [39] copyright 2017 Wiley-VCH).

performed to phase identification. Panel (c) exhibits a typical pattern for the Fe nanocolloid in water, where there are faint halos suggesting a high crystallinity of the NPs. Table in panel (d) presents the labeled ED rings, according to the inter-plane distances $d_{\alpha-Fe}$, $d_{Fe_2O_3}$ and $d_{Fe_3O_4}$, and to the corresponding Miller indices (h, k, l), indexed with reflection lines (JCPDS #06-0696 to $\alpha-Fe$, #75-0033 to Fe_3O_4 and #39-1346 to $\gamma-Fe_2O_3$). The crystallographic parameters of Fe_3O_4, $\gamma-Fe_2O_3$ and $\alpha-Fe$ are obtained from TEM simulation software (JEMS).

The field-dependent magnetization curves at room temperature for the Fe nanocolloids in water and in ethanol are presented in **Figure 12**. The cycles show the common behavior for NPs in a superparamagnetic state.

After a theoretical fitting using the Langevin function (Eq. 1), the log-normal distributions of radii centered at 1.7 nm for water and 3.7 nm for ethanol, are determined (inset in **Figure 12**). In this Figure it is observed that for the nanocolloid in water, the regime of magnetic saturation is not reached even at 18 kOe. This is probably due to surface effects and non-magnetic shells on NPs.

The magnetic saturation of the Fe nanocolloid in water (49.3 e mu g^{-1}) is higher than for the case of ethanol (26.5 emu g^{-1}). In both cases, the saturation magnetization is less than for Fe in bulk size (217 emu g^{-1}) [41]. However, the Fe NPs obtained

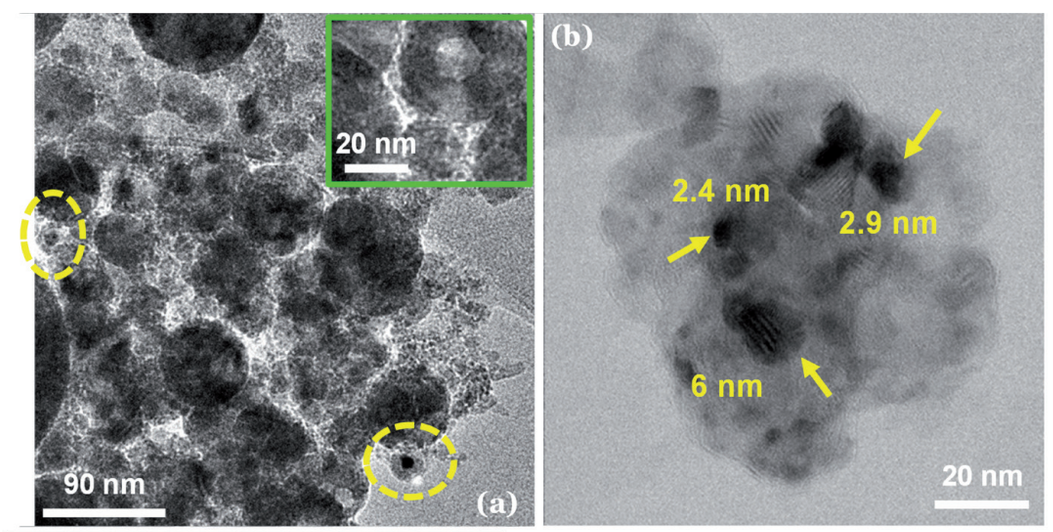

(d)

Line	$d_{\alpha\text{-Fe}}$ [nm]	$d_{Fe_2O_3}$ [nm]	$d_{Fe_3O_4}$ [nm]	(h, k, l)
1			0,299	(0, 2, 2)
2			0,255	(1, 3, 3)
3	0,201			(0, 1, 1)
4		0,184		(0, 2, 4)
5		0,147		(3, 0, 0)

Figure 11.
TEM images of Fe nanocolloids in water (a) and ethanol (b). The images show NPs with spherical structure where the numbers indicate their radius. (c) ED pattern indexed with the reflection lines belonging to Fe_3O_4 (lines 1 and 2), $\alpha-Fe$ (lines 3 and 6) and Fe_2O_3 (lines 4 and 5) according to table (d) for the Fe nanocolloid in water (reprinted with permission from [39] copyright 2017 Wiley-VCH).

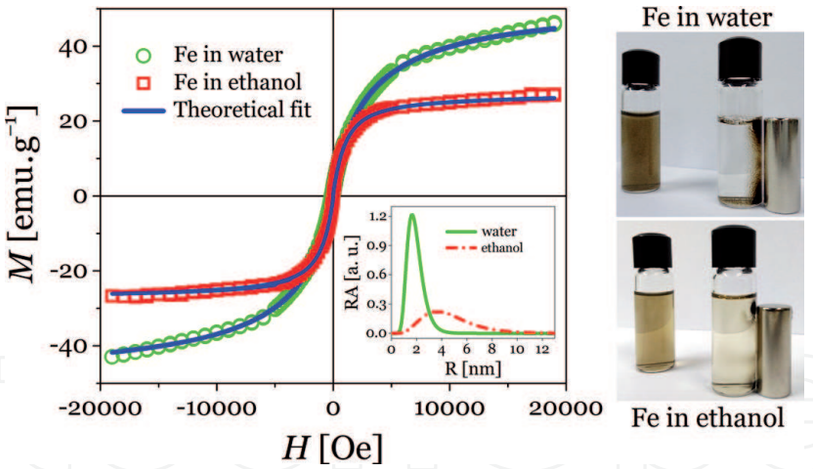

Figure 12.
Experimental magnetization curves and Langevin fitting of Fe nanocolloids in water and in ethanol. The inset shows the size distribution for each nanocolloid. At right: photographs of the colloidal suspensions where the magnetic effect on the NPs exerted by a NdFeB magnet may be observed.

have saturation magnetization greater than that determined by Maneeratanasarn *et al*. [42], who published on the synthesis of magnetic NPs by laser ablation of a target of α - Fe_2O_3 in ethanol, deionized water and acetone.

On the other hand, the smooth change in the magnetization slope in the region close to zero of the applied field, evidences the presence of different oxide phases as previously revealed in the MRS and ED studies.

2.3 Synthesis and characterization of few atoms Ag nanoclusters

Metallic clusters are known as few nanometer sized particles made up of sub-units, which can be atoms of a single element (mono metal), or of several elements (alloys). Their novel chemical and physical properties are dependent only on the number of atoms they contain. These size-dependent properties, which make them suitable for applications in catalysis [43], photoluminescence [44], biomedical [45], magnetism [46], among others, show significant deviations from their bulk and large NPs counterparts. There are different procedures for clusters synthesis, which rely on the use of microemulsions [47], thiol cappings [48], vesicles [49] and electrochemistry techniques [46].

Particularly, Ag NCs have received much attention as novel fluorophores due to their good photostability, high quantum yield emitters and low toxicity. These properties make them suitable for microscopy settings, with potential biocompatibility, applications to sensing and bio-labelling when DNA is used as template [50]. With the experimental setup shown in **Figure 1**, Ag colloidal suspensions containing different sized NPs were obtained. To separate small clusters from the large Ag NPs, the nanocolloids were centrifuged varying centrifugation speed and time [6].

Fluorescence spectra of the as-prepared nanocolloids, normalized to their absorbance at 220 nm, yield band structures in the range 250 nm to 625 nm (**Figure 13(a)**). These bands correspond to transitions arising from a discretization of the energy bands when bulk metal downscale to few atoms structures. According to the jellium model, the HOMO-LUMO bandgap energy ($\mathbf{E}_g$) of the metal cluster, the Fermi energy ($\mathbf{E}_F$) of the bulk metal and the number of atoms (N) in the cluster are related by the expression $\mathbf{E}_g = \mathbf{E}_F \times \mathbf{N}^{-1/3}$ [51, 52]. Considering $\mathbf{E}_F$ = 5.49 eV for Ag, full line in **Figure 13(b)** shows the $\mathbf{E}_g$ relation with N according to this expression, showing a

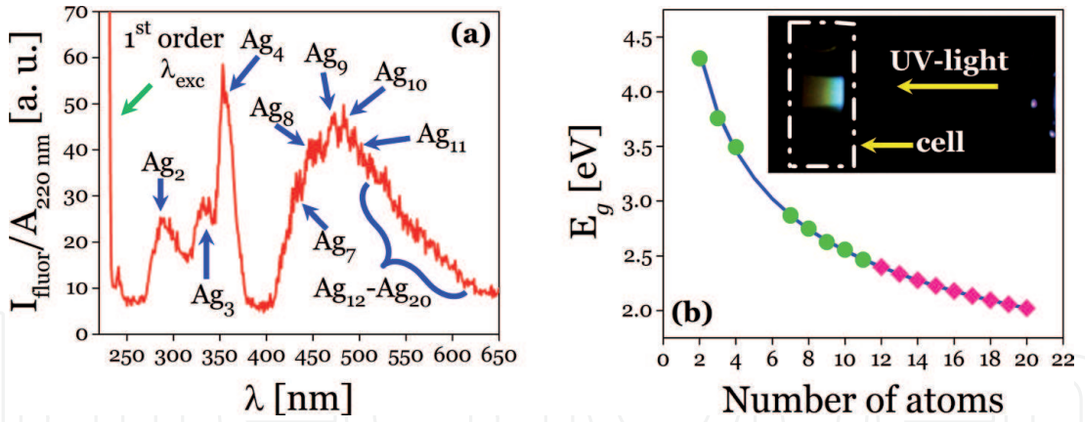

Figure 13.
(a) Fluorescence spectra in the UV-visible region. (b) E_g *vs. N according to the jellium model (full line). Symbols denote observed experimental fluorescence band peaks. Inset shows a snapshot of the induced visible fluorescence on the sample cell [6].*

monotonically decreasing dependence on cluster atoms number. Besides, it is clear that, for increasing N, the $\mathbf{E}_g$ values get closer to each other.

Experimental $\mathbf{E}_g$ values may be estimated from the peak wavelength of the fluorescence UV-visible bands in **Figure 13(a)**. With these values, clusters atom number may be determined from the curve in **Figure 13(b)**, which enables to assign the different band peaks to specific cluster atom numbers (circles and diamonds). In this way, isolated peaks corresponding to $\mathbf{Ag}_2$, $\mathbf{Ag}_3$ and $\mathbf{Ag}_4$ are clearly identified. It is also observed the overlapping of bands for increasing N, giving rise to the observed wide band. Arrows indicate the wavelengths corresponding to $\mathbf{Ag}_7$ to $\mathbf{Ag}_{11}$ NCs. $\mathbf{Ag}_{12}$ to $\mathbf{Ag}_{20}$ are indicated by the curly bracket. Inset in **Figure 13(b)** is a photograph of the visible fluorescence observed in the sample cell when it is illuminated by UV light (220 nm), corresponding to the white band between 400 nm and 625 nm.

When the as-prepared nanocolloids are centrifuged at 15000 rpm with increasing centrifugation times, the bands corresponding to larger NCs disappear, remaining a dominant band at 284 nm, which increases in intensity as centrifugation time increases (**Figure 14**). Inset presents spectra of the as-prepared and 20 min centrifugation samples as well as that for pure water for comparison.

HRTEM analysis using HAADF-STEM mode for image quality improvement on selected parts of the sample is shown in **Figure 15**. Panel (a) shows a panoramic of clusters in different aggregation stages. Coexistence of 1 nm radius NPs together with few atoms NCs is readily observed. In the NPs pointed by yellow arrows, Bragg planes can be observed. Agglomeration of atomic NCs is indicated by dashed green line, while few atoms clusters of 0.1 nm in size are pointed by white arrows. Panel (b) exhibits another site of the sample, with similar formations, including a cluster in a proto-particle stage with crystalline structure but without a defined morphology, enclosed by full blue circle.

Reactivity of NCs is high compared to their bulk counterparts, due to their high surface to volume ratio. Photocatalytic activity of Ag nanocolloid containing mainly small NCs was assessed by degradation of freshly prepared MB. **Figure 16(a)** presents the absorption spectrum of pure MB solution at different time intervals while illuminated by a white light lamp. The main MB absorption band at 660 nm decreases gradually as exposure time elapses showing native dye photocatalytic degradation. **Figure 16(b)** shows the same experiment, but when MB is mixed with the few atoms NCs colloid.

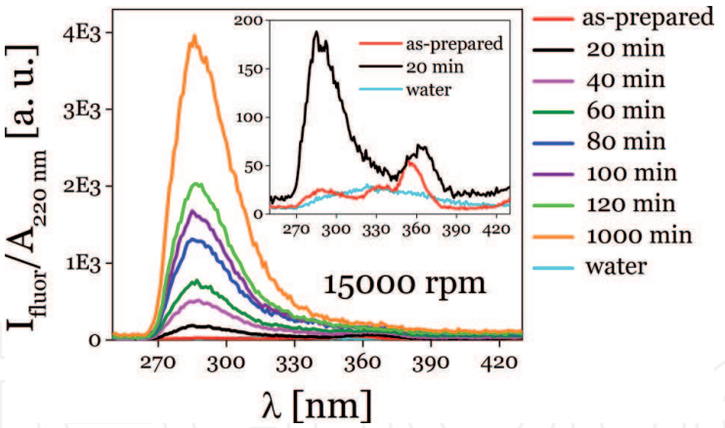

Figure 14.
Fluorescence spectra of nanocolloid obtained by FLASiS (600 μJ pulse energy) of Ag solid target in water for different centrifugation times. Excitation wavelength is $\lambda_{exc} = 220$ nm *. A dominant band at 284 nm is readily seen [6].*

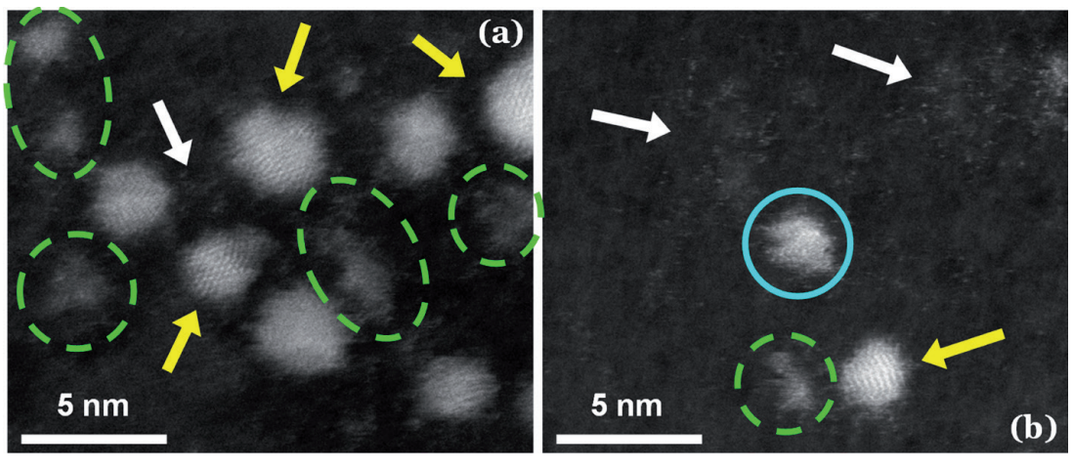

Figure 15.
High resolution and double-corrected electron microscopy analysis in HAADF-STEM mode for NCs observation [6].

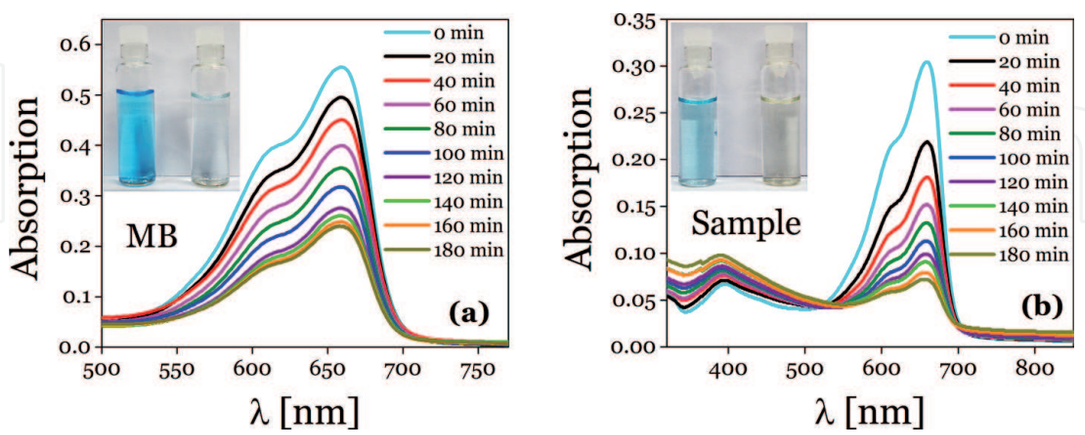

Figure 16.
Degradation of MB. (a) Absorption spectra of pure MB sample illuminated by a white light lamp taken at fixed time intervals. (b) Absorption spectra of sample containing small concentration of NCs under the same conditions as in (a) [6].

The MB absorbance decreases progressively faster than for pure MB. Dye degradation is easily identified by color change in the solution, from deep blue to faint light blue after exposure to white light (insets in the Figures). Degradation efficiency amounts to 80%, while for pure MB is only 55%.

3. Conclusion

FLASiS was used as a "green" method for synthesizing Ag, Ni and Fe metal nanocolloids in liquid media.

Comparison of Ag nanocolloids synthesized by FLASiS and chemical route in aqueous solutions of TSC and st has been discussed. Micro-Raman spectroscopy indicated that stabilizer molecules are adsorbed on the NPs surface and inhibit agglomeration, even up to one year in TSC. FLASiS synthesized NPs seem to stabilize faster that those generated by chemical route, as evidenced by the evolution of their optical extinction spectra.

Magnetic NPs like Ni and Fe colloids were generated in water and *n*-heptane. Spherical NPs shape is almost fully dominant, with a bimodal log-normal size distribution centered at roughly 4 nm and 9 nm radii. Different structures, like hollow type NPs and NiO species were observed. Nanocolloids in *n*-heptane exhibit a greater magnetic response than in water, both showing superparamagnetic behavior.

Fe NPs lack the characteristic optical plasmonic resonance exhibited by noble metals. Raman spectra of the Fe nanocolloids in water and ethanol show Raman peaks of magnetite, hematite or mixtures of them. For the case of water, maghemite signals were also detected.

Few atoms (2–20) Ag NCs can also be synthesized by FLASiS followed by several step centrifugation processes. Fluorescence spectra yield band structures in the range 250 nm to 625 nm, in agreement with the jellium model which predicts HOMO-LUMO type transitions. HRTEM analysis show clusters in different aggregation stages, with coexistence of 1 nm radius NPs together with few atoms NCs. Photocatalytic activity of Ag NCs was assessed against degradation of freshly prepared pure methylene blue. It was found that this efficiency rises 25% in the mixture of Ag NCs and MB.

Acknowledgements

We want to thank Dr. M.B. Fernandez Van Raap and Dr. D. Coral from Instituto de Física de La Plata (IFLP - CONICET) for the VSM measures. Besides, we acknowledge Dr. D. Muraca from Instituto de Física "Gleb Wataghin" (IFGW), Universidade Estadual de Campinas, Brasil and Dr. A. Caneiro from Y-TEC S.A., Argentina, for TEM analysis. We gratefully acknowledge their commitment and dedication.

These works were granted by PIPs 0394, 0280 and 0720 of CONICET, PME 2006-00018, PICTs 2012-1817 and 2016-3205 (ANPCyT), grants 11/I151 and 11/I197 (Facultad de Ingeniería), and 11/X651 and 11/X680 (Facultad de Ciencias Exactas) of Universidad Nacional de La Plata (UNLP), Argentina. We thank C2NANO-Brazilian Nanotechnology National Laboratory (LNNano) at Centro Nacional de Pesquisa em Energia e Materiais (CNPEM)/MCT (#14825, #14827, #16976, #18425, #19927 and #22345) and Research proposal TEM-16976 for the use of TEM. VSM was carried out at IFLP. Synthesis of nanocolloids by FLASiS, and OES, MRS, fluorescence and photocatalysis studies were performed at CIOp (CONICET - CIC - UNLP), La Plata. We acknowledge Y-TEC S.A. for the use of TEM FEI TALOS F200X.

D.C.S. and V.B.A. are researchers of CIC. L.B.S., J.M.J.S. and D.M.A. are researchers of CONICET, Argentina.

Author details

Jesica María José Santillán[1*], David Muñetón Arboleda[1*], Valeria Beatriz Arce[1], Lucía Beatriz Scaffardi[1] and Daniel Carlos Schinca[1,2]

1 Optical Research Center (CIOp, CONICET - CIC - UNLP), La Plata, Buenos Aires, Argentina

2 Engineering Faculty, National University of La Plata, La Plata, Buenos Aires, Argentina

*Address all correspondence to: jesicas@ciop.unlp.edu.ar and davidm@ciop.unlp.edu.ar

IntechOpen

References

[1] Gazit E. Self-assembled peptide nanostructures: the design of molecular building blocks and their technological utilization. Chem Soc Rev. 2007;36:1263-9. DOI: 10.1039/B605536M

[2] Kinkhabwala A, Yu Z, Fan S, Avlasevich Y, Müllen K, Moerner WE. Large single-molecule fluorescence enhancements produced by a bowtie nanoantenna. Nat Photonics. 2009;3:654-7. DOI: 10.1038/nphoton.2009.187

[3] Gao J, Gu H, Xu B. Multifunctional Magnetic Nanoparticles: Design, Synthesis, and Biomedical Applications. Acc Chem Res. 2009;42:1097-107. DOI: 10.1021/ar9000026

[4] Mafuné, F, Kohno J, Takeda Y, Kondow T, Sawabe H. Structure and Stability of Silver Nanoparticles in Aqueous Solution Produced by Laser Ablation. J Phys Chem B. 2000;104:8333-7. DOI: 10.1021/jp001803b

[5] Zhang D, Gökce B, Barcikowski S. Laser Synthesis and Processing of Colloids: Fundamentals and Applications. Chem Rev. 2017;117:3990-4103. DOI: 10.1021/acs.chemrev.6b00468

[6] Santillán JMJ, Muñetón Arboleda D, Muraca D, Schinca DC, Scaffardi LB. Highly fluorescent few atoms silver nanoclusters with strong photocatalytic activity synthesized by ultrashort light pulses. Sci Rep. 2020;10:8217. DOI: 10.1038/s41598-020-64773-z

[7] Pimpang, Pichitchai, Sutham, Withun, Mangkorntong, Nikorn, Mangkorntong, Pongsri, Choopun, Supab. Effect of Stabilizer on Preparation of Silver and Gold Nanoparticle Using Grinding Method. Chiang Mai J Sci. 2008;35:250-7.

[8] Amendola V, Scaramuzza S, Agnoli S, Granozzi G, Meneghetti M, Campo G, et al. Laser generation of iron-doped silver nanotruffles with magnetic and plasmonic properties. Nano Res. 2015;8:4007–DOI: 10.1007/s12274-015-0903-y

[9] Santillán JMJ, Fernández van Raap MB, Mendoza Zélis P, Coral D, Muraca D, Schinca DC. Ag nanoparticles formed by femtosecond pulse laser ablation in water: self-assembled fractal structures. J Nanopart Res. 2015;17:86. DOI: 10.1007/s11051-015-2894-8

[10] Zheng C, Wang H, Liu L, Zhang M, Liang J, Han H. Synthesis and Spectroscopic Characterization of Water-Soluble Fluorescent Ag Nanoclusters. J Anal Met Chem. 2013;2013:e261648. DOI: 10.1155/2013/261648

[11] Riboh JC, Haes AJ, McFarland AD, Ranjit Yonzon C, Van Duyne RP. A Nanoscale Optical Biosensor: Real-Time Immunoassay in Physiological Buffer Enabled by Improved Nanoparticle Adhesion. J Phys Chem B. 2003;107:1772-80. DOI: 10.1021/jp022130v

[12] Abreu AS, Oliveira M, de Sá A, Rodrigues RM, Cerqueira MA, Vicente AA, et al. Antimicrobial nanostructured starch based films for packaging. Carbohyd Polym. 2015;129:127-34. DOI: 10.1016/j.carbpol.2015.04.021

[13] Fernández JG, Almeida CA, Fernández-Baldo MA, Felici E, Raba J, Sanz MI. Development of nitrocellulose membrane filters impregnated with different biosynthesized silver nanoparticles applied to water purification. Talanta. 2016;146:237-43. https://doi.org/10.1016/j.talanta.2015.08.060.

[14] Lara HH, Ayala-Núñez NV, Ixtepan Turrent L del C, Rodríguez Padilla C. Bactericidal effect of silver nanoparticles against multidrug-resistant bacteria. World J Microbiol Biotechnol. 2010;26:615-21. DOI: 10.1007/s11274-009-0211-3

[15] Mori Y, Ono T, Miyahira Y, Nguyen VQ, Matsui T, Ishihara M. Antiviral activity of silver nanoparticle/chitosan composites against H1N1 influenza A virus. Nanoscale Res Lett. 2013;8:93. DOI: 10.1186/1556-276X-8-93

[16] Arboleda DM, Santillán JMJ, Arce VB, Fernández van Raap MB, Muraca D, Fernández MA, et al. A simple and "green" technique to synthesize long-term stability colloidal Ag nanoparticles: Fs laser ablation in a biocompatible aqueous medium. Mater Charact. 2018;140:320-32. DOI: 10.1016/j.matchar.2018.04.021

[17] Bohren CF, Absorption HDR. Absorption and Scattering of Light by Small Particles. John Wiley & Sons; 2008.

[18] Muñetón Arboleda D, Santillán JMJ, Mendoza Herrera LJ, van Raap MBF, Mendoza Zélis P, Muraca D, et al. Synthesis of Ni Nanoparticles by Femtosecond Laser Ablation in Liquids: Structure and Sizing. J Phys Chem C. 2015;119:13184-93. DOI: 10.1021/acs.jpcc.5b03124

[19] Schinca DC, Scaffardi LB, Videla FA, Torchia GA, Moreno P, Roso L. Silver–silver oxide core–shell nanoparticles by femtosecond laser ablation: core and shell sizing by extinction spectroscopy. J Phys D: Appl Phys. 2009;42:215102. DOI: 10.1088/0022-3727/42/21/215102

[20] Santillán JMJ, Scaffardi LB, Schinca DC. Quantitative optical extinction-based parametric method for sizing a single core–shell Ag–Ag_2O nanoparticle. J Phys D: Appl Phys. 2011;44:105104. DOI: 10.1088/0022-3727/44/10/105104

[21] Santillán JMJ, Videla FA, Fernández van Raap MB, Schinca DC, Scaffardi LB. Analysis of the structure, configuration, and sizing of Cu and Cu oxide nanoparticles generated by fs laser ablation of solid target in liquids. J App Phys. 2013;113:134305. DOI: 10.1063/1.4798387

[22] Santillán JMJ, Videla FA, Fernández van Raap MB, Muraca D, Scaffardi LB, Schinca DC. Influence of size-corrected bound-electron contribution on nanometric silver dielectric function. Sizing through optical extinction spectroscopy. J Phys D: Appl Phys. 2013;46:435301. DOI: 10.1088/0022-3727/46/43/435301

[23] Arce VB, Santillán JMJ, Muñetón Arboleda D, Muraca D, Scaffardi LB, Schinca DC. Characterization and Stability of Silver Nanoparticles in Starch Solution Obtained by Femtosecond Laser Ablation and Salt Reduction. J Phys Chem C. 2017;121:10501-13. DOI: 10.1021/acs.jpcc.6b12384

[24] Martina I, Wiesinger R, Jembrih-Simbürger D, Schreiner M. Micro-Raman characterisation of silver corrosion products: instrumental set up and reference database. E-Preserv Sci. 2012;9:1-8.

[25] Vinogradova E, Tlahuice-Flores A, Velazquez-Salazar JJ, Larios-Rodriguez E, Jose-Yacaman M. Surface-enhanced Raman scattering of N-acetylneuraminic acid on silver nanoparticle surface. J Raman Spectrosc. 2014;45:730-5. DOI: 10.1002/jrs.4544

[26] Kizil R, Irudayaraj J, Seetharaman K. Characterization of Irradiated Starches by Using FT-Raman and FTIR Spectroscopy. J Agric Food

Chem. 2002;50:3912-8. DOI: 10.1021/jf011652p

[27] Cael SJ, Koenig JL, Blackwell J. Infrared and raman spectroscopy of carbohydrates: Part III: raman spectra of the polymorphic forms of amylose. Carbohyd Res. 1973;29:123-34. DOI: 10.1016/S0008-6215(00)82075-3

[28] Landázuri N, Tong S, Suo J, Joseph G, Weiss D, Sutcliffe DJ, et al. Magnetic Targeting of Human Mesenchymal Stem Cells with Internalized Superparamagnetic Iron Oxide Nanoparticles. Small. 2013;9:4017-26. DOI: 10.1002/smll.201300570

[29] Orozco-Henao JM, Coral DF, Muraca D, Moscoso-Londoño O, Mendoza Zélis P, Fernandez van Raap MB, et al. Effects of Nanostructure and Dipolar Interactions on Magnetohyperthermia in Iron Oxide Nanoparticles. J Phys Chem C. 2016;120:12796-809. DOI: 10.1021/acs.jpcc.6b00900

[30] Wang Y-XJ. Superparamagnetic iron oxide based MRI contrast agents: Current status of clinical application. Quant Imaging Med Surg. 2011;1:35-40. DOI: 10.3978/j.issn.2223-4292.2011.08.03

[31] Veiseh O, Gunn JW, Zhang M. Design and fabrication of magnetic nanoparticles for targeted drug delivery and imaging. Adv Drug Deliv Rev. 2010;62:284-304. DOI: 10.1016/j.addr.2009.11.002

[32] Park J, Kang E, Son SU, Park HM, Lee MK, Kim J, et al. Monodisperse Nanoparticles of Ni and NiO: Synthesis, Characterization, Self-Assembled Superlattices, and Catalytic Applications in the Suzuki Coupling Reaction. Adv Mater. 2005;17:429-34. DOI: 10.1002/adma.200400611

[33] Xu R, Xie T, Zhao Y, Li Y. Quasi-homogeneous catalytic hydrogenation over monodisperse nickel and cobalt nanoparticles. Nanotech. 2007;18:055602. DOI: 10.1088/0957-4484/18/5/055602

[34] Ramírez-Meneses E, Betancourt I, Morales F, Montiel-PalmaV,Villanueva-AlvaradoCC, Hernández-RojasME.Superparamagnetic nickel nanoparticles obtained by an organometallic approach. J Nanopart Res. 2011;13:365-74. DOI: 10.1007/s11051-010-0039-7

[35] Rodríguez-Llamazares S, Merchán J, Olmedo I, Marambio HP, Muñoz JP, Jara P, et al. Ni/Ni oxides nanoparticles with potential biomedical applications obtained by displacement of a nickel-organometallic complex. J Nanosci Nanotechnol. 2008;8:3820-7. DOI: 10.1166/jnn.2008.199

[36] Solans C, Izquierdo P, Nolla J, Azemar N, Garcia-Celma MJ. Nano-emulsions. Current Opinion in Col Int Sci. 2005;10:102-10. DOI: 10.1016/j.cocis.2005.06.004

[37] Tartaj P, Morales MP, Veintemillas-Verdaguer S, Gonzalez-Carreño T, Serna CJ. chapter 5 Synthesis, Properties and Biomedical Applications of Magnetic Nanoparticles. In: Buschow KHJ, editor. Handbook of Magnetic Materials, vol. 16, Elsevier; 2006, p. 403-82. DOI: 10.1016/S1567-2719(05)16005-3

[38] Zhang D, Tong Z, Li S, Zhang X, Ying A. Fabrication and characterization of hollow Fe3O4 nanospheres in a microemulsion. Mater Lett. 2008;62:4053-5. DOI: 10.1016/j.matlet.2008.05.023

[39] Santillán JMJ, Muñetón Arboleda D, Coral DF, Fernández van Raap MB, Muraca D, Schinca DC, et al. Optical and Magnetic Properties of Fe Nanoparticles Fabricated by Femtosecond Laser Ablation in Organic and Inorganic Solvents.

ChemPhysChem. 2017;18:1192-209. DOI: 10.1002/cphc.201601279

[40] Amendola V, Riello P, Meneghetti M. Magnetic Nanoparticles of Iron Carbide, Iron Oxide, Iron@Iron Oxide, and Metal Iron Synthesized by Laser Ablation in Organic Solvents. J Phys Chem C. 2011;115:5140-6. DOI: 10.1021/jp109371m

[41] Crangle J, Goodman GM, Sucksmith W. The magnetization of pure iron and nickel. Proceedings of the Royal Society of London A Mathematical and Physical Sciences. 1971;321:477-91. DOI: 10.1098/rspa.1971.0044

[42] Maneeratanasarn P, Khai TV, Choi BG, Shim KB. The effect of laser energy on the preparation of iron oxide by a pulsed laser ablation in ethanol. J Korean Crystal Growth and Crystal Technology. 2012;22:134-8. DOI: 10.6111/JKCGCT.2012.22.3.134

[43] Chen W, Chen S. Oxygen Electroreduction Catalyzed by Gold Nanoclusters: Strong Core Size Effects. Angewandte Chemie. 2009;121:4450-3. DOI: 10.1002/ange.200901185

[44] Xu H, Suslick KS. Sonochemical Synthesis of Highly Fluorescent Ag Nanoclusters. ACS Nano. 2010;4:3209-14. DOI: 10.1021/nn100987k

[45] Ostuni E, Chen CS, Ingber DE, Whitesides GM. Selective Deposition of Proteins and Cells in Arrays of Microwells. Langmuir. 2001;17:2828-34. DOI: 10.1021/la001372o

[46] Santiago González B, Rodríguez MJ, Blanco C, Rivas J, López-Quintela MA, Gaspar Martinho JM. One step synthesis of the smallest photoluminescent and paramagnetic PVP-protected gold atomic clusters. Nano Lett. 2010;10:4217-21. DOI: 10.1021/nl1026716

[47] Buceta D, Piñeiro Y, Vázquez-Vázquez C, Rivas J, López-Quintela MA. Metallic Clusters: Theoretical Background, Properties and Synthesis in Microemulsions. Catalysts. 2014;4:356-74. DOI: 10.3390/catal4040356

[48] Donkers RL, Lee D, Murray RW. Synthesis and Isolation of the Molecule-like Cluster Au38(PhCH2CH2S)24. Langmuir. 2008;24:5976-5976. DOI: 10.1021/la801163t

[49] Wu, Zeng, Schelly ZA. Growth of Uncapped, Subnanometer Size Gold Clusters Prepared via Electroporation of Vesicles. J Phys Chem B. 2005;109:18715-8. DOI: 10.1021/jp0543476

[50] Yuan Z, Chen Y-C, Li H-W, Chang H-T. Fluorescent silver nanoclusters stabilized by DNA scaffolds. Chem Commun. 2014;50:9800-15. DOI: 10.1039/C4CC02981J

[51] Haberland H, editor. Clusters of Atoms and Molecules: Theory, Experiment, and Clusters of Atoms. Berlin Heidelberg: Springer-Verlag; 1994. DOI: 10.1007/978-3-642-84329-7

[52] Kreibig U, Vollmer M. Optical Properties of Metal Clusters. Berlin Heidelberg: Springer-Verlag; 1995. DOI: 10.1007/978-3-662-09109-8